Air plasma sprayed high-entropy AlCoCrFeNiY coating with excellent oxidation and spallation resistance under cyclic oxidation at 1050–1150 °C

DOI:
10.1016/j.corsci.2022.110151

Air plasma sprayed high-entropy AlCoCrFeNiY coating with excellent oxidation and spallation resistance under cyclic oxidation at 1050-1150 °C

Jie Lu [a], Ying Chen [b], Zihao Sun [a], Ling Li [a], Xuanzhen Liu [a], Aihui Huang [a], Han Zhang [a], Fangwei Guo [a], Xiancheng Zhang [c], Xiaofeng Zhao [a,*]

[a] Shanghai Key Laboratory of Advanced High-Temperature Materials and Precision Forming, School of Materials Science and Engineering, Shanghai Jiao Tong University, Shanghai, 200240, China

[b] Department of Materials and the Henry Royce Institute, The University of Manchester, Manchester M13 9PL, United Kingdom

[c] Key Laboratory of Pressure Systems and Safety, Ministry of Education, School of Mechanical and Power Engineering, East China University of Science and Technology, Shanghai, 200237, China

Abstract

An AlCoCrFeNiY high-entropy alloy coating was prepared using air plasma spray. The cyclic oxidation behavior of the coating was investigated and compared with that of a conventional NiCoCrAlY coating. It is demonstrated that the AlCoCrFeNiY coating exhibits much stronger resistance to oxidation and spallation than the NiCoCrAlY coating when they are thermally cycled between room temperature and 1050-1150 °C. The difference is attributed to a much lower growth rate of the oxide scale on the AlCoCrFeNiY coating as a result of its significantly higher activation energy of oxidation and the absence of spinel.

Keywords: High-entropy alloy; Metallic coating; Thermal spraying; Oxidation; High temperatures

*Corresponding author: Xiaofeng Zhao (xiaofengzhao@sjtu.edu.cn)

1. Introduction

Overlay coatings based on NiCoCrAlY alloys are commonly applied onto critical components (e.g., turbine blades, nozzles and combust chambers) of gas turbine engines to protect the metallic substrates against oxidation and improve their bonding to ceramic thermal barrier coatings. The oxidation resistance of NiCoCrAlY coatings relies on their capabilities to form an adherent, continuous and dense oxide scale (predominantly α-Al_2O_3) upon high temperature exposure [1-4]. The oxides develop large thermal mismatch stress in cooling, which drives cracking and spallation of the oxides. Apart from α-Al_2O_3, transient oxides (e.g. $(Ni,Co)(Cr,Al)_2O_4$) may form in the early oxidation stage of the NiCoCrAlY coatings. The transient oxides are less protective, fast growing and degrade the interfacial adhesion, thus accelerating the failure of the oxides [5, 6]. The service temperature of NiCoCrAlY coatings is generally lower than 1050 °C due to their fast oxide growth rates and interface degradation at higher temperatures [5-8]. Therefore, coatings with higher temperature capabilities than NiCoCrAlY will be required to meet the continuous demand for a higher thrust-weight ratio of gas turbines.

High-entropy alloys (HEAs), also referred to as multi-principal element alloys containing five or more principal elements, have attracted the huge interest of the materials science community due to their unique structure and excellent properties [9-12]. In the HEAs family, $Al_xCoCrFeNi$ HEAs are one of the most studied alloys because they show high structural flexibility and their properties are adjustable by tailoring the Al content [13-15]. Among the $Al_xCoCrFeNi$ HEAs, equimolar AlCoCrFeNi HEA exhibits superior specific strength at high temperatures and has been considered as a potential candidate for high temperature applications [16]. More importantly, AlCoCrFeNi HEA is expected to have good oxidation resistance due to its high concentration of Al, which provides an Al reservoir for growth of Al_2O_3, and characteristic nanostructure, which offers fast outward diffusion paths for Al to feed the growth of Al_2O_3 [4]. In our previous works [17, 18], we designed a new, reactive element (RE) doped AlCoCrFeNi HEA and showed that the alloy had excellent

oxidation and spallation resistance by forming a continuous, slowly growing and adherent Al_2O_3 scale. In addition, the oxidation rate of the RE-doped AlCoCrFeNi HEA at 1100 °C is one magnitude lower than those of the conventional NiCoCrAlY alloys. Given such exceptional performances in oxidation, the RE-doped AlCoCrFeNi HEA is considered as a promising overlay coating material for applications at temperatures higher than 1050 °C.

In our recent work [19], we manufactured a RE-doped AlCoCrFeNi coating by spark plasma sintering (SPS) and found it showed superior performance in isothermal oxidation at 1100 °C. These preliminary results have demonstrated that the RE-doped AlCoCrFeNi HEA coating has huge potential for oxidation protection at high temperatures. However, SPS is not a viable technique for coating deposition in most industry applications. [20, 21]. As a result, if AlCoCrFeNi HEA coatings are to be used for gas turbines, they would be likely manufactured by a widely used deposition technique such as air plasma spray (APS) and have different oxidation behavior due to the significant difference in microstructure between SPS and APS coatings [22, 23]. In addition, while we have shown the RE-doped AlCoCrFeNi coating has an extremely low oxidation rate in isothermal oxidation, it is still unknown whether the thermally grown oxide is resistant to spallation during thermal cycling.

In this study, we extended our previous work to a RE-doped AlCoCrFeNi HEA coating deposited by APS. Cyclic oxidation was carried out between room temperature and three different peak temperatures (1050 °C, 1100 °C and 1150 °C) to test the performance of the coating (e.g., oxidation kinetics and resistance to oxide spallation) against a benchmark NiCoCrAlY coating at temperatures higher than 1050 °C. Extensive characterizations on microstructure, composition and residual stress were performed to support the comparison and understand the oxidation mechanisms.

2. Materials and method

2.1. AlCoCrFeNiY powder preparation

The equimolar Al, Co, Cr, Fe and Ni metals with an addition of 0.5 wt% Y were used

as raw materials. All materials with their nominal composition were put into a medium frequency induction furnace for melting. The melting process was repeated three times to ensure chemical homogeneity. Finally, a cylindrical ingot of ~6kg were obtained. The ingot was crushed into small particles with a diameter of 1-3mm. Then, the particle size was further reduced in a planetary ball mill at a rotation speed of 400 rpm for 10 min. Finally, the milling powder was sieved into a size range from 45 to 85 μm for coating deposition.

2.2. Coating preparation

An industry benchmark NiCoCrAlY coating and an AlCoCrFeNiY high-entropy alloy coating were deposited on Hastalloy-X alloy (Ni-22Cr-18Fe-9Mo-1.5W-0.1C in wt%) substrates using a supersonic plasma spray system (HEPJ-II; National Key Laboratory for Remanufacturing, Beijing, China). The substrates were grit blasted to increase the surface roughness and ultrasonically cleaned for 15 minutes before the plasma spray. The AMDRY 365-2 powder (Oerlikon Metco, Westbury, NY) with the composition (wt%) Ni-22Co-16.7Cr-12.3Al-0.5Y was utilized to prepare the NiCoCrAlY coating. For the AlCoCrFeNiY coating, an intermediate NiCoCrAlY coating (100 ± 30 μm in thickness) was deposited between AlCoCrFeNiY coating and substrate to enhance the interfacial bonding. The two types of coatings were deposited using the same spraying parameters, which were listed in Table 1. Finally, the chemical composition and microstructure of the two coatings were homogenized by heat treatment at 1100 °C for 2 h in vacuum ($<10^{-5}$ Pa).

2.3. Cyclic oxidation test

The AlCoCrFeNiY and NiCoCrAlY coated Hastalloy-X were cut into cuboid samples (10 mm × 10 mm × 4 mm) using a SiC cutting blade in a precision cut-off machine (Accutom 5, Struers). Prior to cyclic oxidation testing, the coatings of all the samples were ground to a thickness of about 400 ± 30 μm and subsequently polished to a 0.05 μm finish to eliminate the effect of surface roughness on oxidation. The samples

were then thermally cycled between room temperature and a peak temperature of 1050 °C, 1100 °C and 1150 °C, respectively, in laboratory air using an automatically controlled circulating heating furnace. Each cycle consisted of 1 h exposure at the peak temperature and 10 min fan-assisting cooling.

2.4 Samples characterization

The composition and microstructure of the coating and oxide scale were analyzed by a scanning electron microscope (SEM, Mira3, Tescan) fitted with energy dispersive X-ray spectroscopy (EDS, Oxford Instruments). The composition and structure of each phase in the as-homogenized AlCoCrFeNiY coatings were studied by a scanning transmission electron microscope (STEM, Talos F200X G2, Thermo Fisher Scientific, USA) and EDS. The sample for STEM analysis was in the form of thin lamella with a size of about 10 μm (length) × 5 μm (width) × 50 nm (thickness) and was prepared by a focused ion beam (FIB, GAIA3, Tescan, Czech Republic). The residual stress in the thermally grown alumina scale was measured at room temperature in ambient air using the photoluminescence piezospectroscopy (PLPS) with a green 532 nm Nd:YAG laser based on a confocal Raman microprobe (LabRAM HR, Horiba Jobin Yvon, France).

3. Results

3.1. Coating microstructure

Fig. 1 shows the cross-sectional microstructure of the as-homogenized AlCoCrFeNiY coating. A typical lamellar structure resulted from thermal spray can be observed in Fig. 1a, b and e. According to the magnified BSE images taken from different regions of the coating (Fig. 1c and f), the AlCoCrFeNiY coating consists of γ phase, β phase, nano-sized precipitates in the β matrix and thin Al_2O_3 layers between laminae because of the in-flight oxidation of powder during spraying. According to the Fig. 1c with corresponding Y map in Fig. 1d, it can be found that the Y-rich oxides are also formed in the regions of Al_2O_3 formation due to a higher oxygen affinity of Y than Al [24]. Apart from Y in the Y-rich oxides and solid solution of Y in alloy, other Y in the form

of Y-rich intermetallic compounds (bright nano-sized particles in Fig. 1c and f) is distributed in coating matrix [25]. Due to the post-process heat treatment, an inter-diffusion zone (IDZ) develops at the NiCoCrAlY coating/substrate interface (Fig. 1g). Fig.2 presents the TEM analysis of the as-homogenized AlCoCrFeNiY coating. The coating comprises the FCC-structured γ phase (bright contrast), the B2-structured β phase (dark contrast) and the nanosized A2 precipitates in the β matrix based on the conjoint analysis of the HAADF-STEM images and SAED patterns (Fig. 2a, b and c). Meanwhile, the Y-rich precipitates with bright contrast (Y-rich intermetallic compounds) are further identified and confirmed by STEM-EDX maps of Y. According to the STEM-EDX elemental mapping (Fig. 2d and e), the γ phase is NiCoCrFe-rich and the β is NiCoAl-rich, while the A2 phase is enriched with Fe, Co and Cr. The specific element composition of each phase determined from the STEM-EDX point analysis is summarized in Table 2. For the as-sprayed AlCoCrFeNi alloy, the alloy show a two-phase coherent structure that comprises A2 and B2 (β) [16]. Therefore, the formation of γ phase in the AlCoCrFeNiY coating originates from the thermodynamic equilibrium process during the post-deposition heat treatment [13, 18]. The benchmark NiCoCrAlY coating (Fig. 3) has a similar thickness with the AlCoCrFeNiY coating and is composed of NiCoCr-rich γ phase (bright contrast) and NiAl-rich β phase (dark contrast). An IDZ layer is also formed at the coating/substrate interface.

3.2. Oxidation behavior

Fig. 4 gives an overview of the NiCoCrAlY and AlCoCrFeNiY coating surface after cyclic oxidation for different time at 1050 °C, 1100 °C and 1150 °C, respectively. The exposed metal surface represents the region that has undergone oxide scale spallation. For the NiCoCrAlY coating, catastrophic oxide scale spallation occurs after cyclic oxidation (Fig. 4a, b, c and g). The relative surface area in which spallation occurs exceeds 40 % after 800 cycles at 1050 °C, 80 % after 100 cycles at 1100 °C and 90 % after 50 cycles at1150 °C, respectively. For the AlCoCrFeNiY coating (Fig. 4d, e, f and g), the oxide scale is intact and almost no oxide scale spallation can be observed after

1000 cycles at 1050 °C, 500 cycles at 1100 °C and 200 cycles at1150 °C, respectively. It should be noted that the NiCoCrAlY coating surface shows blue color while the AlCoCrFeNiY coating surface shows a relatively grey color. According to our previous works [26, 27], the blue color represents the formation of spinel. In short, the AlCoCrFeNiY coating show much stronger resistance to oxide spallation than those of the NiCoCrAlY coating in thermal cycling.

Fig. 5 shows the surface morphology of the NiCoCrAlY coating after cyclic oxidation at 1050 °C, 1100 °C and 1150 °C, respectively. The exposed metal surface indicates that the spallation of the oxide scale occurs along the scale/coating interface. A layer of spinel is identified on the surface of the area where spallation has not occurred (Fig. 5a, c and e). Based on the SEM-EDX point analysis (Fig. 5b, d and f) and the site preference of elements in spinel structure, the chemical formula of the spinel is likely to be (Ni, Co)(Al, Cr)$_2$O$_4$. Similar results are also reported in previous studies [4, 26].

Fig. 6 shows the cross-sectional microstructure of the NiCoCrAlY coating after cyclic oxidation at 1050 °C, 1100 °C and 1150 °C, respectively. First, the oxide scale formed on the NiCoCrAlY coating at three temperatures has a double-layer structure, consisting of an outer spinel oxide layer and an inner Al_2O_3 layer (Fig. 6b, d, f and g), which agree well with the observations in Fig. 5. Second, the Ni plating can be clearly seen at the scale/coating interface. This result suggests that some parts of the oxide scale were already detached from the interface after oxidation. Third, as Al reservoir in the coating is gradually consumed by oxidation and interdiffusion, an Al-depletion layer and an IDZ are identified underneath the oxide scale and at the coating/substrate interface, respectively. But the β phase in the mixed region of γ and β phases is still sufficient to support the growth of Al_2O_3 (Fig. 6b, d and f). Therefore, the formation of spinel oxides layer for the NiCoCrAlY coating occurs in the early oxidation stage [4].

Fig. 7 shows the surface morphology of the AlCoCrFeNiY coating after cyclic oxidation at 1050 °C, 1100 °C and 1150 °C. The AlCoCrFeNiY coating is fully covered by a continuous, uniform oxide scale, suggesting good interfacial adhesion between the oxide and the coating (Fig. 7a, c and e). Based on the SEM-EDX point analysis (Fig.

7b, d and f), the external oxide scale is a $(Al,Cr,Fe)_2O_3$ formation, primarily comprising Al_2O_3 with minor Cr and Fe in solid solution. In addition, some Y-rich oxides are randomly dispersed on the scale surface. Unlike the NiCoCrAlY coating, spinel is not found on the AlCoCrFeNiY coating after oxidation.

Fig. 8 shows the cross-sectional microstructure of the AlCoCrFeNiY coating after cyclic oxidation at 1050 °C, 1100 °C and 1150 °C. First, a uniform and continuous oxide scale develops on the AlCoCrFeNiY coating at three temperatures and no interfacial delamination can be observed (Fig. 8a, e and f). Second, the oxide scale after oxidation at 1100 °C and 1150 °C predominantly consists of an inner Al_2O_3 layer and a thin, outer $(Al,Cr,Fe)_2O_3$ layer, which is consistent with the observations from the oxide surface (Fig. 8b, d, f, h, j and l). However, the outer $(Al,Cr,Fe)_2O_3$ layer is not seen on the cross-section of the AlCoCrFeNiY coating after oxidation at 1050 °C, probably due to a much lower thickness or a low concentration of Cr and Fe (Fig. 7b, Fig 8b and d). Third, the consumption of Al resulting from the oxide growth and the formation of IDZ causes dissolution of A2 phase but growth of γ phase, thus leading to a double-phase structure (γ and β phases) eventually (Fig. 8c, g and k). It should be emphasized that no detrimental precipitates form at the AlCoCrFeNiY/NiCoCrAlY coating interface, which suggests a good chemical compatibility between two coatings (Fig. 8c, g and k). In other words, the intermediate NiCoCrAlY coating not only enhances the interfacial bonding, but also avoids a direct interaction of the AlCoCrFeNiY coating with the superalloy substrate, which might be a good design strategy to fully realize the excellent oxidation performance of RE-doped AlCoCrFeNi alloy.

3.3. Oxidation kinetics

The oxidation rate plays an important role in failure of oxide scales. Fig. 9 summaries the oxidation kinetics of the NiCoCrAlY coating and the AlCoCrFeNiY coating at 1050 °C, 1100 °C and 1150 °C, respectively. Fig. 9a and b plot the thickness of the oxide scale as a function of square root of oxidation time. The linear fitting to each set of data points suggests that the oxide growth for the two coatings follows a parabolic

law [28]:

$$h^2 = k_p t \quad (1)$$

where k_p, h and t are the oxidation rate constant, the thickness of the oxide scale and the oxidation time, respectively.

The calculated oxidation rate constants for the NiCoCrAlY coating are 4.7×10^{-14} cm^2/s at 1050 °C, 6.0×10^{-13} cm^2/s at 1100 °C and 1.3×10^{-12} cm^2/s at 1150 °C, respectively (Fig. 9a). Based on the results reported by Evans et al. [29], the oxidation rate constant of an APS CoNiCrAlY coating at 1100 °C ranges from 3×10^{-13} cm^2/s to 16×10^{-13} cm^2/s, and thus the oxidation rate constant of the NiCoCrAlY coating at 1100 °C (6.0×10^{-13} cm^2/s) is close to the lower bound of the reported value. For the AlCoCrFeNiY coating, the oxidation rate constants are 1.0×10^{-14} cm^2/s at 1050 °C, 2.2×10^{-13} cm^2/s at 1100 °C and 8.3×10^{-13} cm^2/s at 1150 °C, respectively (Fig. 9b). Compared with NiCoCrAlY coating, the oxidation rates of the AlCoCrFeNiY coating are 79% lower at 1050 °C, 63% lower at 1100 °C and 36% lower at 1150 °C, respectively.

The activation energy of oxidation is usually utilized to achieve a further understanding on the oxidation mechanism of alloys. Once the oxidation of alloys is performed under the linearly increasing temperatures with a single oxidation process, the activation energy of oxidation can be calculated within the corresponding temperature range using the Arrhenius equation [30, 31]:

$$k_p = k_0 \exp\left(\frac{-Q}{RT}\right) \quad (2)$$

where k_0 is a constant, while Q, R and T are the activation energy of oxidation, the gas constant (8.314 J/(mol.k)) and the temperature, respectively. *Therefore, the* activation energy of oxidation for the AlCoCrFeNiY coating is calculated to be 694.8 kJ/mol at 1050-1150 °C, which is 37% higher than that (506.7 kJ/mol) of NiCoCrAlY coating (Fig. 9c). According to the results reported by Fritscher and Schulz et al. [32, 33]*, the* activation energies of oxidation for NiCoCrAlY-type coatings are commonly fall within the range of 356-510 kJ/mol at 1000-1200 °C, which includes the activation energy of oxidation for NiCoCrAlY coating in this study. It should be pointed out that the activation energies for NiCoCrAlY-type bond coats were obtained from a complete

TBC system. Since YSZ is oxygen transparent, the effect of the top coat on the activation energy of oxidation should be negligible. However, the composition and microstructure of substrates and NiCoCrAlY-type bond coats can also affect the growth of oxide scales, thus giving rise to variation of activation energy from study to study. However, the activation energy of oxidation for the AlCoCrFeNiY coating at 1050-1150 °C significantly exceeds the upper bound of the activation energy for NiCoCrAlY-type bond coats. The much higher activation energy of oxidation for the AlCoCrFeNiY coating represents a much stronger resistance to growth of oxides, which lowers the oxidation rate. The underlying mechanism for the high activation energy of oxidation for the AlCoCrFeNiY coating will be discussed later.

4. Discussion

4.1. Understanding on the oxidation resistance

For the NiCoCrAlY coating, the oxide scale consists of an outer spinel layer ((Ni, Co)(Al,Cr)$_2$O$_4$) and an inner Al_2O_3 layer in contact with the metal (Fig. 6). Compared with the Al_2O_3, spinel is fast growing and thus increases the oxidation rate. In addition, formation of spinel in oxidation is detrimental to interfacial adhesion (especially for the YSZ TBCs) due to its intrinsic brittleness [4, 34]. The high content of the Al-rich β phase in the β/γ mixed region of the NiCoCrAlY coating supports the continuous growth of Al_2O_3. For this reason, the spinel layer comes from the early oxidation stage of the coating (Fig. 6b, d and f). The initial Al concentration at the NiCoCrAlY coating surface is insufficient to support the formation of a continuous, external Al_2O_3 scale in early oxidation stage, and thus other metal elements (e.g., Ni, Co and Cr) are oxidized to form transient oxides due to a high oxygen partial pressure. Meanwhile, spinel forms by the solid reaction between Al_2O_3 and the transient oxides [4, 23, 29]. The formation and thickening of a continuous spinel oxide layer cause a rapid decrease in the oxygen partial pressure at the scale/coating interface, which subsequently favors the formation of Al_2O_3. Eventually, the thickening of the oxide scale on the NiCoCrAlY coating is governed by the growth of Al_2O_3 during the long-term oxidation.

For the AlCoCrFeNiY coating, a $(Al,Cr,Fe)_2O_3$ layer, rather than $(Ni, Co)(Al, Cr)_2O_4$, forms at the top of the oxide scale. This result indicates that the formation of detrimental spinel is effectively suppressed by the AlCoCrFeNiY coating. In this study, the Al concentration (12.3 wt%) in the NiCoCrAlY coating is higher than that (10.7wt%) in the AlCoCrFeNiY coating, but the AlCoCrFeNiY coating exhibits a preferential Al_2O_3 formation. This can only be explained by the unique composition or microstructure of the AlCoCrFeNiY coating, which play an important role in facilitating the formation of Al_2O_3. Firstly, the nanostructure significantly increases the number of grain boundaries, which accelerates the outward Al diffusion to form Al_2O_3 [4, 35]. The original A2/β nanostructure in the AlCoCrFeNiY coating introduces large quantities of phase boundaries, which promotes the growth of Al_2O_3 (Fig. 1 and 2). In the meantime, the $(Al,Cr,Fe)_2O_3$ phase is formed by the solid state reaction between the initially grown Cr_2O_3, Fe_2O_3 and Al_2O_3. It should be mentioned that the Cr (< 5at%) and Fe (< 1at%) contents are extremely low in $(Al,Cr,Fe)_2O_3$, and thus $(Al,Cr,Fe)_2O_3$ is still Al_2O_3-based. It is hypothesized that the formation of minor Cr_2O_3 and Fe_2O_3 results from the early oxidation of the FeCr-rich γ phase and the nanosized, FeCr-rich A2 phase. However, the growth of Cr_2O_3 and Fe_2O_3 is quickly inhibited due to the high Al diffusion rate, thus limiting their low contents in $(Al,Cr,Fe)_2O_3$. According to previous works [36, 37], the hexagonal Cr_2O_3 and Fe_2O_3 could be served as the nucleation sites for α-Al_2O_3 because they are isostructural to α-Al_2O_3. Similar template effect is also found in a NiAl alloy with a certain amount of Cr and a FeAl alloy coated by Cr and Fe films [36, 38]. Therefore, it is proposed that the initially grown Cr_2O_3 and Fe_2O_3 in the early oxidation stage are nucleation sites for formation and growth of α-Al_2O_3, thus contributing to a strong inhibiting effect on the formation of spinel.

For the NiCoCrAlY and AlCoCrFeNiY coatings, the thickening of the oxide scale during the long-term oxidation is predominantly controlled by growth of Al_2O_3 (Fig. 6 and 8). It has to be specially noted that the activation energy of oxidation for AlCoCrFeNiY coating is 694.8 kJ/mol at 1050-1150 °C, which is much higher than that (506.7 kJ/mol) of NiCoCrAlY coating (Fig. 9c) in the same temperature range. For the

polycrystalline Al_2O_3-forming alloys, the overall diffusion flux of Al to form Al_2O_3 is governed by the fluxes through the bulk lattice and grain boundaries, which can be expressed as [4]:

$$D_{Al} = D_{Al}^{L}(1 - f) + D_{Al}^{GB} f \quad (3)$$

where D_{Al}^{L} and D_{Al}^{GB} are diffusion coefficients of Al through the lattice and along the grain boundaries, respectively. f is the area ratio of the grain boundaries. For a long-term oxidation process, the Al diffusion flux from grain boundaries should have no obvious difference between the NiCoCrAlY and AlCoCrFeNiY coatings due to their comparable grain sizes (1-5μm) (Fig. 1-3). The contribution of the grain size of A2 phase to Al diffusion flux in the AlCoCrFeNiY coating can be neglected, because both the NiCoCrAlY and AlCoCrFeNiY coatings comprise γ and β phases during long-term oxidation (Fig. 6 and 8). Therefore, the difference in diffusion flux of Al reaching the oxide/metal interface is determined by the lattice diffusion. In addition, the lattice diffusivity might approach the grain boundary diffusivity at a high enough temperature (> 0.6Tm) [39].

For a multi-principal-element HEA, each site in lattice has a different bond configuration due to the different atom surroundings, which causes different lattice potential energy for each lattice site. The significantly fluctuated lattice potential energy in HEA results in a high activation energy for diffusion and thus a low diffusion rate (also termed as elemental sluggish diffusion effect) [40, 41]. In this study, the diffusion flux of Al through the lattice of AlCoCrFeNiY is likely to be reduced by the sluggish diffusion effect of Al element, which leads to a much higher activation energy of oxidation, thus a low oxidation rate. One may argue that if the diffusion flux of Al is decreased in the AlCoCrFeNiY coating, the diffusion fluxes of other metal elements would increase, thus leading to the formation of mixed oxides. However, our experimental observations have shown the oxide scale consists of predominantly Al_2O_3. Two possible reasons might explain this result. First, the diffusion fluxes of all elements in the AlCoCrFeNiY coating are decreased, but Al still has the fastest diffusion rate, which sustains the growth of Al_2O_3. Second, the oxides of other metal elements are not

thermodynamically stable due to the extremely low oxygen partial pressure at the scale/coating, thus resulting in the formation of an exclusive Al_2O_3. Based on the discussion above, the much lower oxidation rates for the AlCoCrFeNiY coating at 1050 °C, 1100 °C and 1150 °C are attributed to the absence of spinel oxides and the much higher activation energy of oxidation.

4.2. Understanding on the spallation resistance

It is widely accepted that the spallation of an oxide scale is governed by the elastic strain energy stored in the oxide scale (the driving force for the spallation of the oxide scale) G, which is proportional to the square of residual stress, σ^2, in the oxide scale and the thickness of oxide scale, h_{ox} [42-44]:

$$G = \frac{(1-v_{ox}^2)\sigma^2 h_{ox}}{2E_{ox}} \quad (4)$$

where E_{ox} and v_{ox} are the Young' modulus and the Poisson' ratio of the oxide scale, respectively. Once the driving force for spallation exceeds the interfacial toughness, the oxide scale will detach from the coating surface. The residual stress in the oxide scale predominantly comes from the mismatch of thermal expansion between the oxide scale and the substrate and the lateral growth of the oxide scale at high temperatures [45-47]. Meanwhile, the residual stress can be measured at room temperature using the PLPS technique, by [43, 47]

$$\Delta v = 5.07\sigma \quad (5)$$

where Δv is the peak shift of Al_2O_3 with respect to the stress-free debris from the spalled Al_2O_3 scale. Fig. 10 shows the evolution of residual stress in oxide scales formed on the NiCoCrAlY and AlCoCrFeNiY coating as a function of oxidation time at 1050 °C, 1100 °C and 1150 °C. The difference in residual stress in the oxide scale between the NiCoCrAlY and AlCoCrFeNiY coating is negligible. For example, the stress levels for the two coatings are about -4.3 GPa, -5.4 GPa and -6.3 GPa after cooling from 1050 °C, 1100 °C and 1150 °C, respectively. Under this circumstance, the driving force for spallation is determined by the thickness of the oxide scale according to the Eq (4). In addition, it is well demonstrated that doping of reactive element Y can

significantly improve the interfacial adhesion of the oxide scale to the coating [48, 49]. Therefore, the interfacial toughness for the two coatings is considered comparable due to the same Y content. It should be noted that the Y concentration of the AlCoCrFeNiY HEA coating and the NiCoCrAlY coating (0.5 wt.%) in this study exceeds the solid solution of Y in both coatings. The reason for adding extra Y is to compensate the loss of Y consumed due to the in-flight oxidation during spraying [49]. Even though some Y is consumed during the APS deposition, the remaining metallic Y (in the form of solid solution and Y-rich intermetallic compounds) can still ensure it gets involved and takes effect in oxidation (Fig. 1, Fig. 2 and Fig. 3). According to the dynamic-segregation theory [48, 50], the dynamical segregation of Y ions from the metallic Y to the oxide/metal interface can suppress the formation of interfacial pores, thus improving the scale adhesion. Additionally, the dynamical segregation of Y ions along Al_2O_3 scale grain boundaries can effectively block the outward Al diffusion, thus lowering the oxidation rate. In our previous work [43], it has been well demonstrated that the formation of nano-sized Y_2O_3 in a same NiCoCrAlY alloy can strengthen the spallation resistance of oxide scale by suppressing the formation of Y-rich oxide inclusions at scale interface and lowering the oxidation rate. In short, a much lower oxidation rate results in a much lower oxide thickness for the AlCoCrFeNiY coating, which leads to significantly lower elastic strain energy in the scale and a superior resistance to oxide spallation.

5. Outlook

The high-entropy AlCoCrFeNiY coating prepared by APS exhibits an ultra-strong oxidation and spallation resistance at 1050-1150 °C, which is highly superior to the conventional NiCoCrAlY coating. Retention of the desirable composition and microstructure of the AlCoCrFeNiY coating are crucial to ensuring its oxidation performance at high temperatures. Therefore, it is proposed that an intermediate NiCoCrAlY layer between the AlCoCrFeNiY coating and the superalloy substrate should be necessary to avoid their direct interaction. In addition, it is also indicated that

no detrimental precipitates develop at the AlCoCrFeNiY/NiCoCrAlY coating interface, which reveals a good chemical compatibility between two coatings (Fig. 8c, g and k). However, the interaction mechanism between the AlCoCrFeNiY coating and NiCoCrAlY coating deserves a further study for optimizing the thickness ratio of two coatings, which will be reported in our future work. In summary, the AlCoCrFeNiY coating can be considered as a new bond coat for TBCs for higher temperature applications due to its superior oxidation performance.

6. Conclusions

An APS high-entropy AlCoCrFeNiY coating with superior cyclic oxidation performance at 1050 °C, 1100 °C and 1150 °C is reported in this study. The oxidation behavior of AlCoCrFeNiY coating is systematically investigated and compared with a benchmark NiCoCrAlY coating. The following conclusions can be drawn.

(1) The AlCoCrFeNiY coating prior to oxidation consists of FCC-structured γ phase, B2-structured β phase and nanostructured A2 precipitates. However, the AlCoCrFeNiY coating is composed of γ phase and β phase after prolonged oxidation. The transformation originates from the growing oxide scale and the elemental inter-diffusion with superalloy substrate. The β phase transforms into γ phase gradually in oxidation due to the constant Al consumption.

(2) In the early oxidation stage of the AlCoCrFeNiY coating, the A2/β nanostructure significantly increases the phase boundary density, which accelerates the outward Al diffusion and thus facilitates the formation of Al_2O_3. In addition, the initially grown Cr_2O_3 and Fe_2O_3 act as nucleation sites for growth of α-Al_2O_3, thus promoting a fast establishment of a thermally stable α-Al_2O_3 scale. As a result, formation of detrimental spinel is suppressed, which improves the mechanical stability of the oxide scale.

(3) For the prolonged oxidation process, the thickening of the oxide scales for both types of coatings is predominantly governed by growth of Al_2O_3. The AlCoCrFeNiY coating exhibits a much higher activation energy of oxidation (694.8 kJ/mol) at 1050-

1150 °C than the NiCoCrAlY coating (506.7 kJ/mol). Such high activation energy of oxidation for the AlCoCrFeNiY coating is attributed to the low diffusion rate of Al.

(4) The absence of spinel growth in the early oxidation stage and the high activation energy of oxidation during the prolonged oxidation contribute to a much lower oxidation rate and much stronger resistance to oxide spallation for the AlCoCrFeNiY coating in comparison to the NiCoCrAlY coating.

Acknowledgements

This work was financially supported by National Natural Science and Foundation of China (51971139 and 52102072).

References

[1] N.P. Padture, M. Gell, E.H. Jordan, Thermal barrier coatings for gas-turbine engine applications, Science, 296 (2002) 280-284.

[2] J.T. DeMasi-Marcin, D.K. Gupta, Protective coatings in the gas turbine engine, Surf. Coat. Technol., 68-69 (1994) 1-9.

[3] G.W. Goward, Progress in coatings for gas turbine airfoils, Surf. Coat. Technol., 108-109 (1998) 73-79.

[4] Y. Chen, X. Zhao, P. Xiao, Effect of microstructure on early oxidation of MCrAlY coatings, Acta Mater., 159 (2018) 150-162.

[5] G.-H. Meng, H. Liu, M.-J. Liu, T. Xu, G.-J. Yang, C.-X. Li, C.-J. Li, Highly oxidation resistant MCrAlY bond coats prepared by heat treatment under low oxygen content, Surf. Coat. Technol., 368 (2019) 192-201.

[6] G.-H. Meng, H. Liu, P.-Y. Xu, G.-R. Li, T. Xu, G.-J. Yang, C.-J. Li, Superior oxidation resistant MCrAlY bond coats prepared by controlled atmosphere heat treatment, Corros. Sci., 170 (2020).

[7] M.J. Pomeroy, Coatings for gas turbine materials and long term stability issues, Materials & Design, 26 (2005) 223-231.

[8] F. Cao, B. Tryon, C.J. Torbet, T.M. Pollock, Microstructural evolution and failure

characteristics of a NiCoCrAlY bond coat in “hot spot” cyclic oxidation, Acta Mater., 57 (2009) 3885-3894.

[9] D.B. Miracle, O.N. Senkov, A critical review of high entropy alloys and related concepts, Acta Mater., 122 (2017) 448-511.

[10] X. Gao, Y. Lu, B. Zhang, N. Liang, G. Wu, G. Sha, J. Liu, Y. Zhao, Microstructural origins of high strength and high ductility in an AlCoCrFeNi2.1 eutectic high-entropy alloy, Acta Mater., 141 (2017) 59-66.

[11] Z. Li, K.G. Pradeep, Y. Deng, D. Raabe, C.C. Tasan, Metastable high-entropy dual-phase alloys overcome the strength-ductility trade-off, Nature, 534 (2016) 227-230.

[12] Y. Zhang, T.T. Zuo, Z. Tang, M.C. Gao, K.A. Dahmen, P.K. Liaw, Z.P. Lu, Microstructures and properties of high-entropy alloys, Prog. Mater Sci., 61 (2014) 1-93.

[13] W.-R. Wang, W.-L. Wang, S.-C. Wang, Y.-C. Tsai, C.-H. Lai, J.-W. Yeh, Effects of Al addition on the microstructure and mechanical property of AlxCoCrFeNi high-entropy alloys, Intermetallics, 26 (2012) 44-51.

[14] J.C. Rao, H.Y. Diao, V. Ocelík, D. Vainchtein, C. Zhang, C. Kuo, Z. Tang, W. Guo, J.D. Poplawsky, Y. Zhou, P.K. Liaw, J.T.M. De Hosson, Secondary phases in AlxCoCrFeNi high-entropy alloys: An in-situ TEM heating study and thermodynamic appraisal, Acta Mater., 131 (2017) 206-220.

[15] Q. Tian, G. Zhang, K. Yin, W. Wang, W. Cheng, Y. Wang, The strengthening effects of relatively lightweight AlCoCrFeNi high entropy alloy, Mater. Charact., 151 (2019) 302-309.

[16] K.R. Lim, K.S. Lee, J.S. Lee, J.Y. Kim, H.J. Chang, Y.S. Na, Dual-phase high-entropy alloys for high-temperature structural applications, J. Alloys Compd., 728 (2017) 1235-1238.

[17] J. Lu, Y. Chen, H. Zhang, L. Li, L. Fu, X. Zhao, F. Guo, P. Xiao, Effect of Al content on the oxidation behavior of Y/Hf-doped AlCoCrFeNi high-entropy alloy, Corros. Sci., 170 (2020) 108691.

[18] J. Lu, Y. Chen, H. Zhang, N. Ni, L. Li, L. He, R. Mu, X. Zhao, F. Guo, Y/Hf-doped

AlCoCrFeNi high-entropy alloy with ultra oxidation and spallation resistance, Corros. Sci., (2020) 108426.

[19] J. Lu, L. Li, Y. Chen, X. Liu, X. Zhao, F. Guo, P. Xiao, Y-Hf co-doped AlCoCrFeNi high-entropy alloy coating with superior oxidation and spallation resistance at 1100 °C, Corros. Sci., 182 (2021).

[20] F. Nozahic, C. Estournès, A.L. Carabat, W.G. Sloof, S. van der Zwaag, D. Monceau, Self-healing thermal barrier coating systems fabricated by spark plasma sintering, Mater. Des., 143 (2018) 204-213.

[21] A.H. Pakseresht, A.H. Javadi, M. Bahrami, F. Khodabakhshi, A. Simchi, Spark plasma sintering of a multilayer thermal barrier coating on Inconel 738 superalloy: Microstructural development and hot corrosion behavior, Ceram. Int., 42 (2016) 2770-2779.

[22] K.A. Kane, M.J. Lance, M. Sweet, B.A. Pint, The effect of bond coating surface modification on the performance of atmospheric plasma spray thermal barrier coatings, Surf. Coat. Technol., 378 (2019).

[23] G.-H. Meng, H. Liu, P.-Y. Xu, G.-R. Li, T. Xu, G.-J. Yang, C.-J. Li, Superior oxidation resistant MCrAlY bond coats prepared by controlled atmosphere heat treatment, Corros. Sci., 170 (2020) 108653.

[24] T.J. Nijdam, L.P.H. Jeurgens, J.H. Chen, W.G. Sloof, On the Microstructure of the Initial Oxide Grown by Controlled Annealing and Oxidation on a NiCoCrAlY Bond Coating, Oxid. Met., 64 (2005) 355-377.

[25] T.J. Nijdam, W.G. Sloof, Effect of Y Distribution on the Oxidation Kinetics of NiCoCrAlY Bond Coat Alloys, Oxid. Met., 69 (2007) 1-12.

[26] J. Lu, H. Zhang, Y. Chen, X. Zhao, F. Guo, P. Xiao, Effect of microstructure of a NiCoCrAlY coating fabricated by high-velocity air fuel on the isothermal oxidation, Corros. Sci., 159 (2019) 108126.

[27] L. Luo, X. Shan, Z. Zou, C. Zhao, X. Wang, A. Zhang, X. Zhao, F. Guo, P. Xiao, A high performance NiCoCrAlY bond coat manufactured using laser powder deposition, Corros. Sci., 126 (2017) 356-365.

[28] C. Wagner, Theoretical Analysis of the Diffusion Processes Determining the Oxidation Rate of Alloys, J. Electrochem. Soc., 99 (1952) 369-380.

[29] H.E. Evans, M.P. Taylor, Diffusion Cells and Chemical Failure of MCrAlY Bond Coats in Thermal-Barrier Coating Systems, Oxid. Met., 55 (2001) 17-34.

[30] P.E.R. Kofstad, Oxidation of Metals: Determination of Activation Energies, Nature, 179 (1957) 1362-1363.

[31] M.P. Agustianingrum, U. Lee, N. Park, High-temperature oxidation behaviour of CoCrNi medium-entropy alloy, Corros. Sci., 173 (2020) 108755.

[32] U. Schulz, K. Fritscher, A. Ebach-Stahl, Cyclic behavior of EB-PVD thermal barrier coating systems with modified bond coats, Surf. Coat. Technol., 203 (2008) 449-455.

[33] K. Fritscher, U. Schulz, C. Leyens, Lifetime-determining spalling mechanisms of NiCoCrAlRE/EB-PVD zirconia TBC systems, Materialwiss. Werkstofftech., 38 (2007) 734-746.

[34] D.R. Clarke, C.G. Levi, Materials Design for the Next Generation Thermal Barrier Coatings, Annual Review of Materials Research, 33 (2003) 383-417.

[35] Z. Liu, W. Gao, K.L. Dahm, F. Wang, Oxidation behaviour of sputter-depositedNi–Cr–Al micro-crystalline coatings, Acta Mater., 46 (1998) 1691-1700.

[36] M.W. Brumm, H.J. Grabke, The oxidation behaviour of NiAl-I. Phase transformations in the alumina scale during oxidation of NiAl and NiAl-Cr alloys, Corros. Sci., 33 (1992) 1677-1690.

[37] Y. Huang, X. Peng, X.-Q. Chen, TiO_2 nanoparticles-assisted α-Al_2O_3 direct thermal growth on nickel aluminide intermetallics: Template effect of the oxide with the hexagonal oxygen sublattice, Corros. Sci., 153 (2019) 109-117.

[38] Y. Kitajima, S. Hayashi, T. Nishimoto, T. Narita, S. Ukai, Rapid Formation of α-Al_2O_3 Scale on an Fe–Al Alloy by Pure-Metal Coatings at 900 °C, Oxid. Met., 73 (2009) 375-388.

[39] H. Peng, H. Guo, J. He, S. Gong, Oxidation and diffusion barrier behaviors of double-layer NiCoCrAlY coatings produced by plasma activated EB-PVD, Surf. Coat.

Technol., 205 (2011) 4658-4664.

[40] K.Y. Tsai, M.H. Tsai, J.W. Yeh, Sluggish diffusion in Co–Cr–Fe–Mn–Ni high-entropy alloys, Acta Mater., 61 (2013) 4887-4897.

[41] M.C. Gao, J.-W. Yeh, P.K. Liaw, Y. Zhang, High-Entropy Alloys Fundamentals and Applications, Springer International Publishing, 2016.

[42] J.W. Hutchinson, M.Y. He, A.G. Evans, The influence of imperfections on the nucleation and propagation of buckling driven delaminations, Journal of the Mechanics and Physics of Solids, 48 (2000) 709-734.

[43] J. Lu, Y. Chen, C. Zhao, H. Zhang, L. Luo, B. Xu, X. Zhao, F. Guo, P. Xiao, Significantly improving the oxidation and spallation resistance of a MCrAlY alloy by controlling the distribution of yttrium, Corros. Sci., 153 (2019) 178-190.

[44] R.W. Jackson, D.M. Lipkin, T.M. Pollock, Thermal barrier coating adherence to Hf-modified B2 NiAl bond coatings, Acta Mater., 80 (2014) 39-47.

[45] V.K. Tolpygo, D.R. Clarke, Alumina scale failure resulting from stress relaxation, Surf. Coat. Technol., 120-121 (1999) 1-7.

[46] L. Qiu, F. Yang, W. Zhang, X. Zhao, P. Xiao, Effect of Al content on the lifetime of thermally grown oxide formed on Ni–Al alloys after isothermal oxidation, Corros. Sci., 89 (2014) 13-20.

[47] R.J. Christensen, V.K. Tolpygo, D.R. Clarke, The influence of the reactive element yttrium on the stress in alumina scales formed by oxidation, Acta Mater., 45 (1997) 1761-1766.

[48] B.A. Pint, Experimental observations in support of the dynamic-segregation theory to explain the reactive-element effect, Oxid. Met., 45 (1996) 1-37.

[49] D. Naumenko, B.A. Pint, W.J. Quadakkers, Current Thoughts on Reactive Element Effects in Alumina-Forming Systems: In Memory of John Stringer, Oxid. Met., 86 (2016) 1-43.

[50] K.A. Unocic, C.M. Parish, B.A. Pint, Characterization of the alumina scale formed on coated and uncoated doped superalloys, Surf. Coat. Technol., 206 (2011) 1522-1528.

Figures and captions

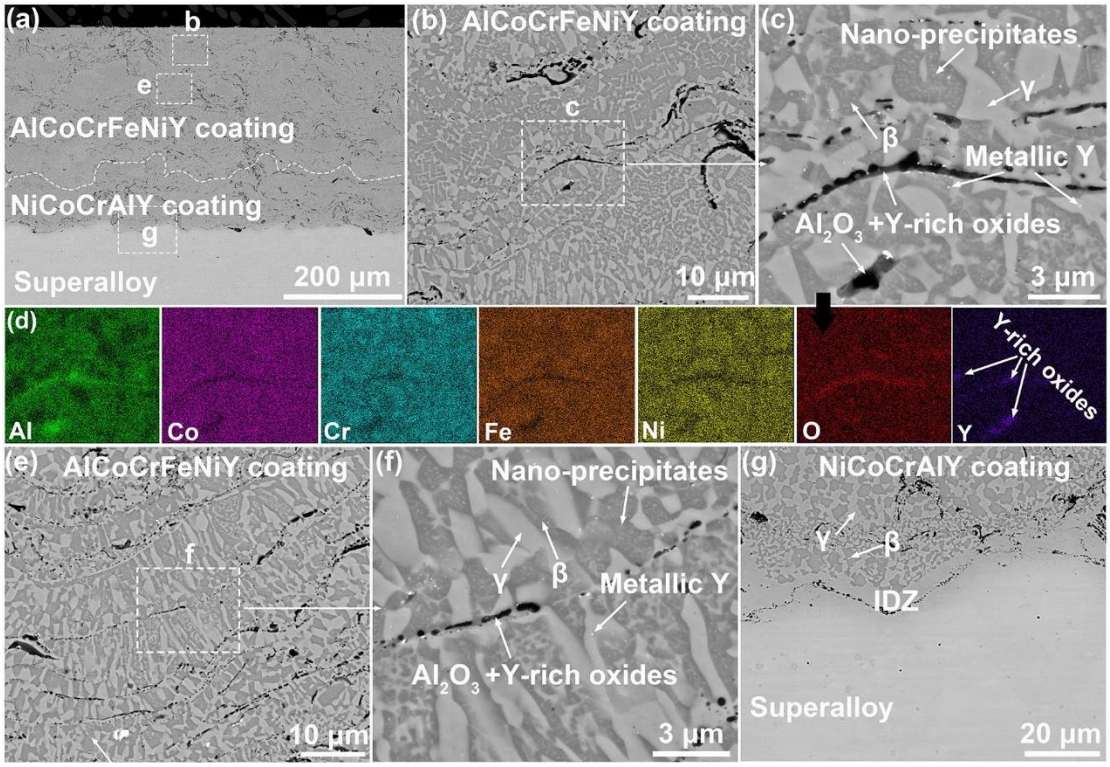

Fig.1 Cross-sectional microstructure and composition of the as-homogenized AlCoCrFeNiY coating: (a) an overview of the cross-sectional microstructure; (b, c and d) the microstructure and composition near the coating surface; (e, f) the microstructure in the middle region of the coating; (g) the microstructure at the NiCoCrAlY coating/substrate interface.

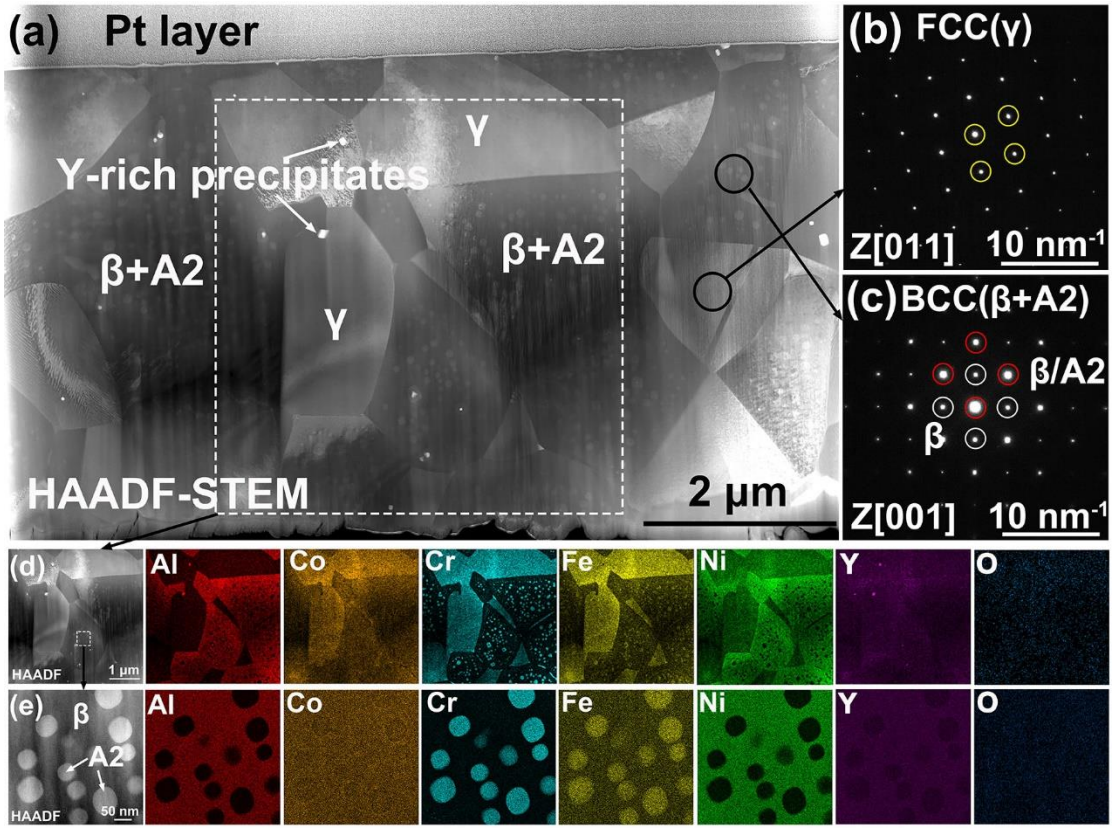

Fig. 2 TEM analysis of the as-homogenized AlCoCrFeNiY coating structure: (a) a high-angle annular dark-field (HAADF) STEM image and (b, c) the corresponding selected-area diffraction (SAED) patterns of γ phase and β phase; (d, e) magnified HAADF-STEM images with the corresponding EDX maps, showing the elemental partitioning to each phase.

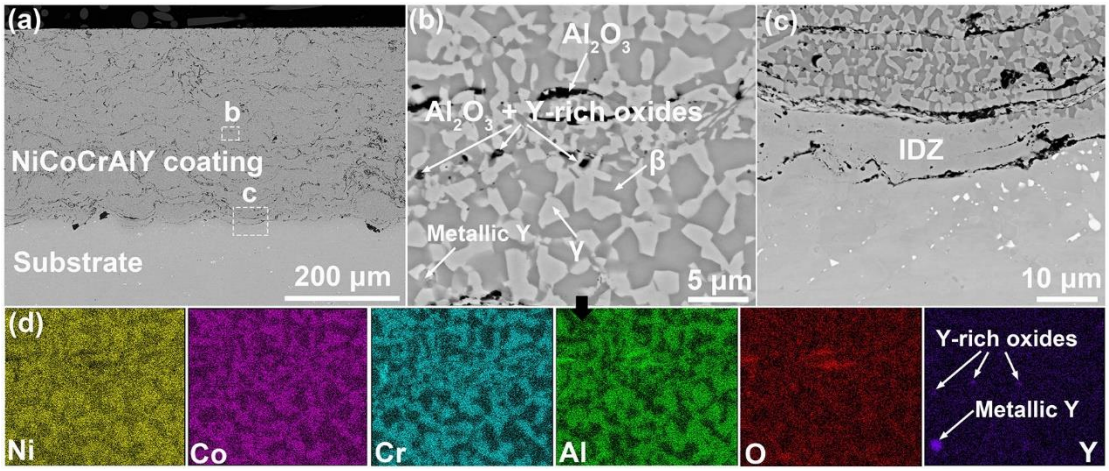

Fig. 3 Cross-sectional microstructure of the NiCoCrAlY coating: (a) an overview of the cross-sectional microstructure; (b, c and d) detailed analysis of phase structure and composition.

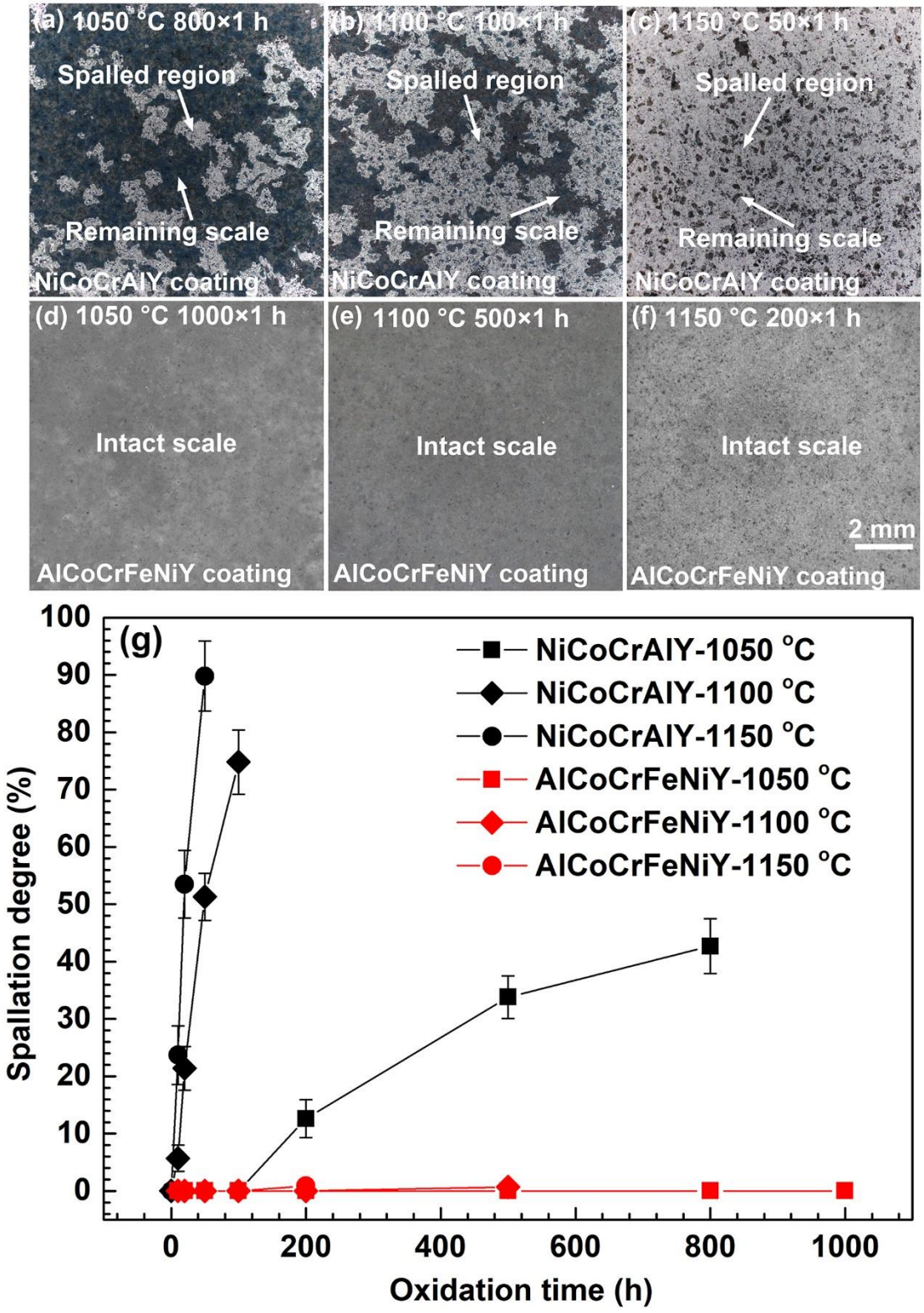

Fig. 4 (a-f) Optical images of NiCoCrAlY coating and AlCoCrFeNiY coating surface after cyclic oxidation for different time at 1050 °C, 1100 °C and 1150 °C; (g) spallation degree of oxide scale formed on the NiCoCrAlY coating and AlCoCrFeNiY coating as a function of oxidation time at 1050 °C, 1100 °C and 1150 °C. (The spallation degree

is defined by the ratio of the exposed metal surface to the whole coating surface. Five optical images with a magnification of 50× are employed to measure the average spallation degree using Image J software and meanwhile the error bar is the standard deviation.)

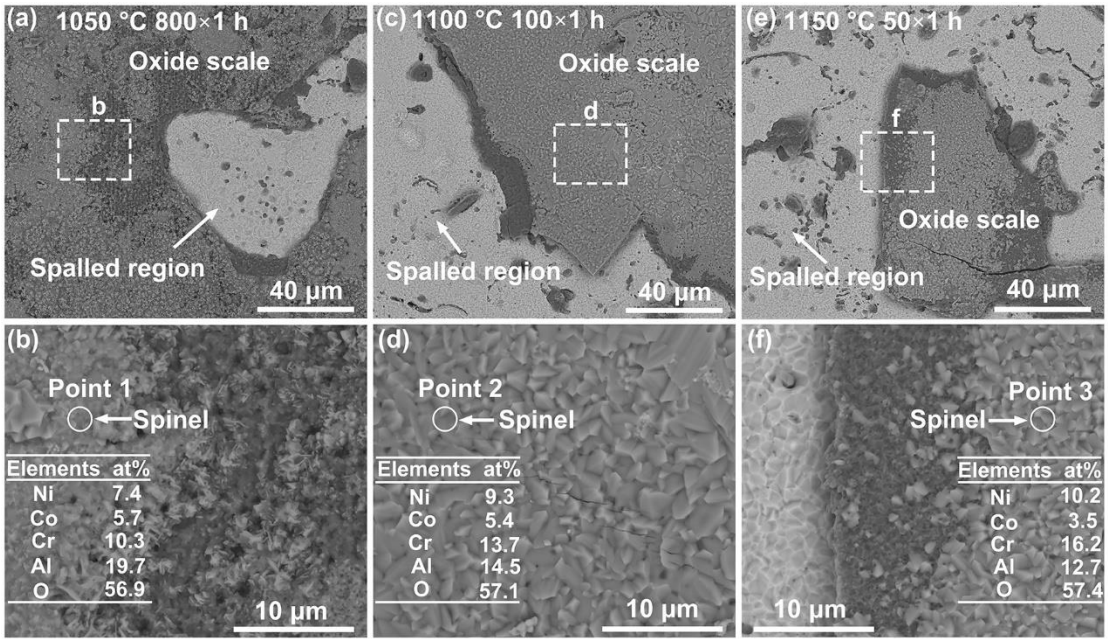

Fig. 5 Surface morphology of NiCoCrAlY coating after cyclic oxidation: (a, b) 1050 °C, 800×1 h; (c, d) 1100 °C, 100×1 h; (e, f) 1150 °C, 50×1 h.

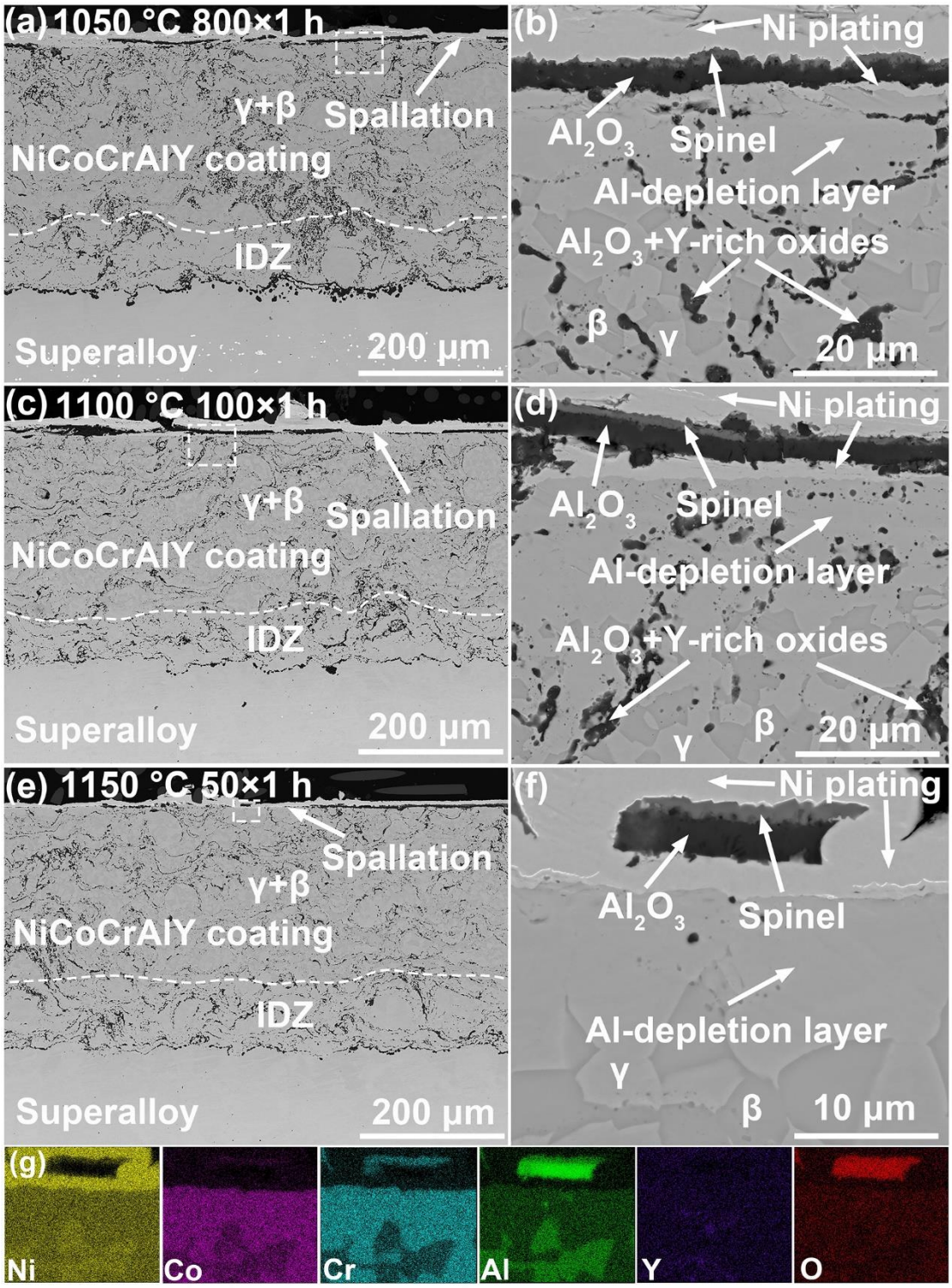

Fig. 6 Cross-sectional morphology and composition of NiCoCrAlY coating after cyclic oxidation: (a, b) 1050 °C, 800×1 h; (c, d) 1100 °C, 100×1 h; (e, f) 1150 °C, 50×1 h; (g) SEM-EDX maps, showing the composition of the oxide scale in (f).

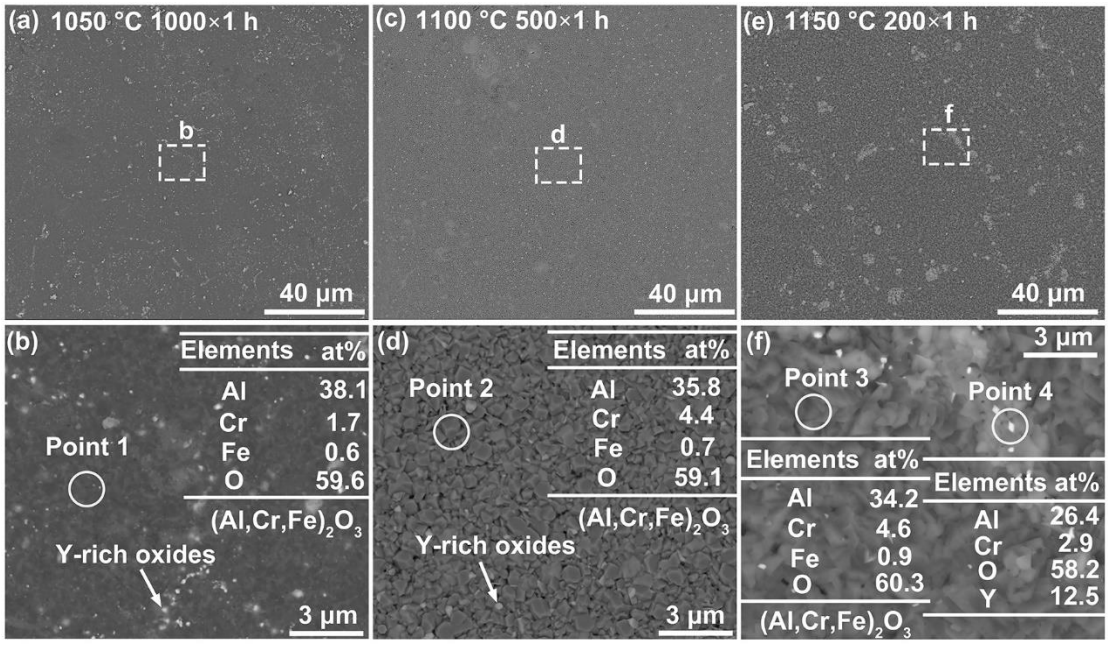

Fig. 7 Surface morphology of AlCoCrFeNiY coating after cyclic oxidation: (a, b) 1050 °C, 1000×1 h; (c, d) 1100 °C, 500×1 h; (e, f) 1150 °C, 200×1 h.

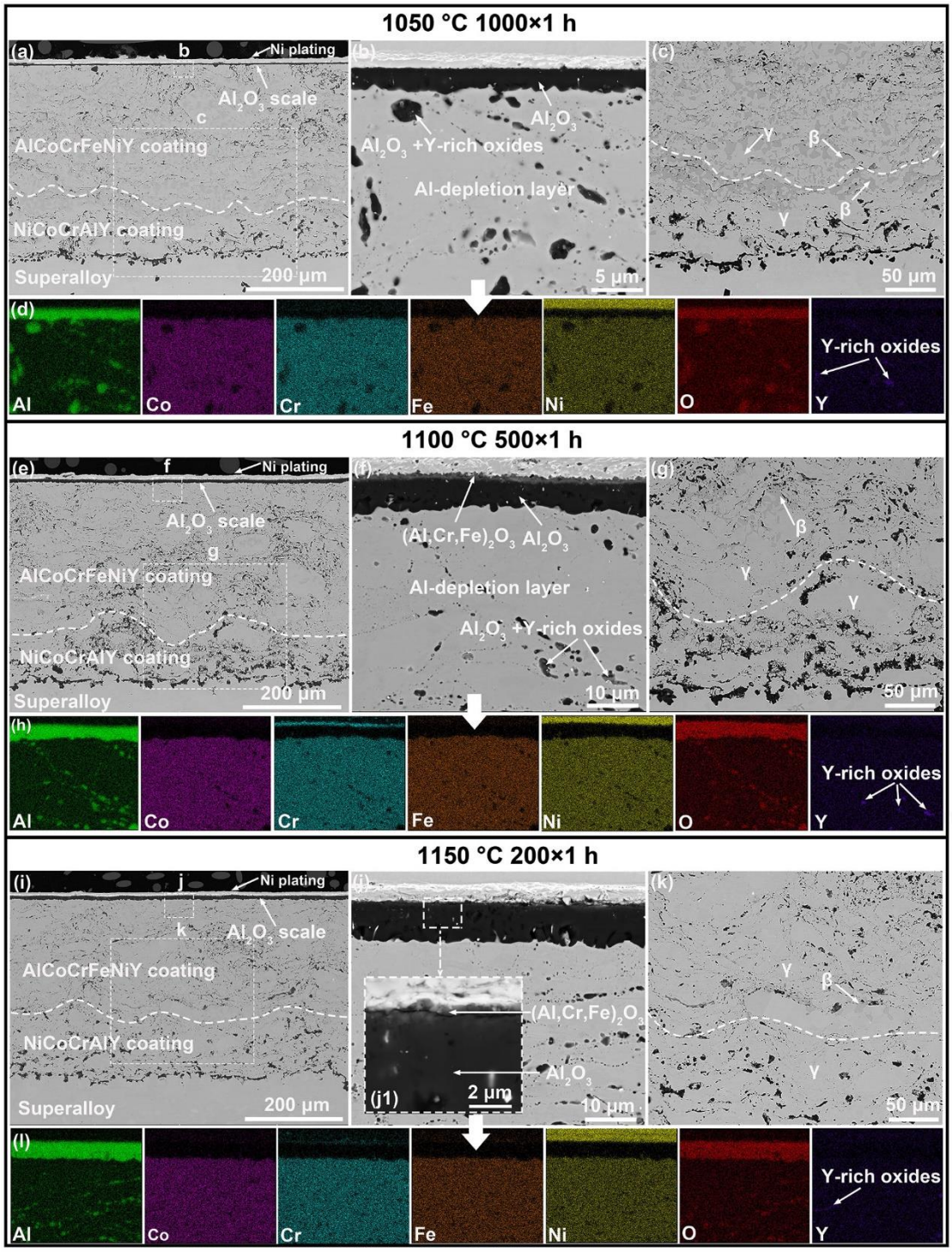

Fig. 8 Cross-sectional microstructure of the AlCoCrFeNiY coating after cyclic oxidation: (a, b and c) 1050 °C, 1000×1 h; (e, f and g) 1100 °C, 500×1 h; (i, j and k) 1150 °C, 200×1 h; (d, h and l) SEM-EDX maps, showing the composition of the oxide scale in (b, f and j).

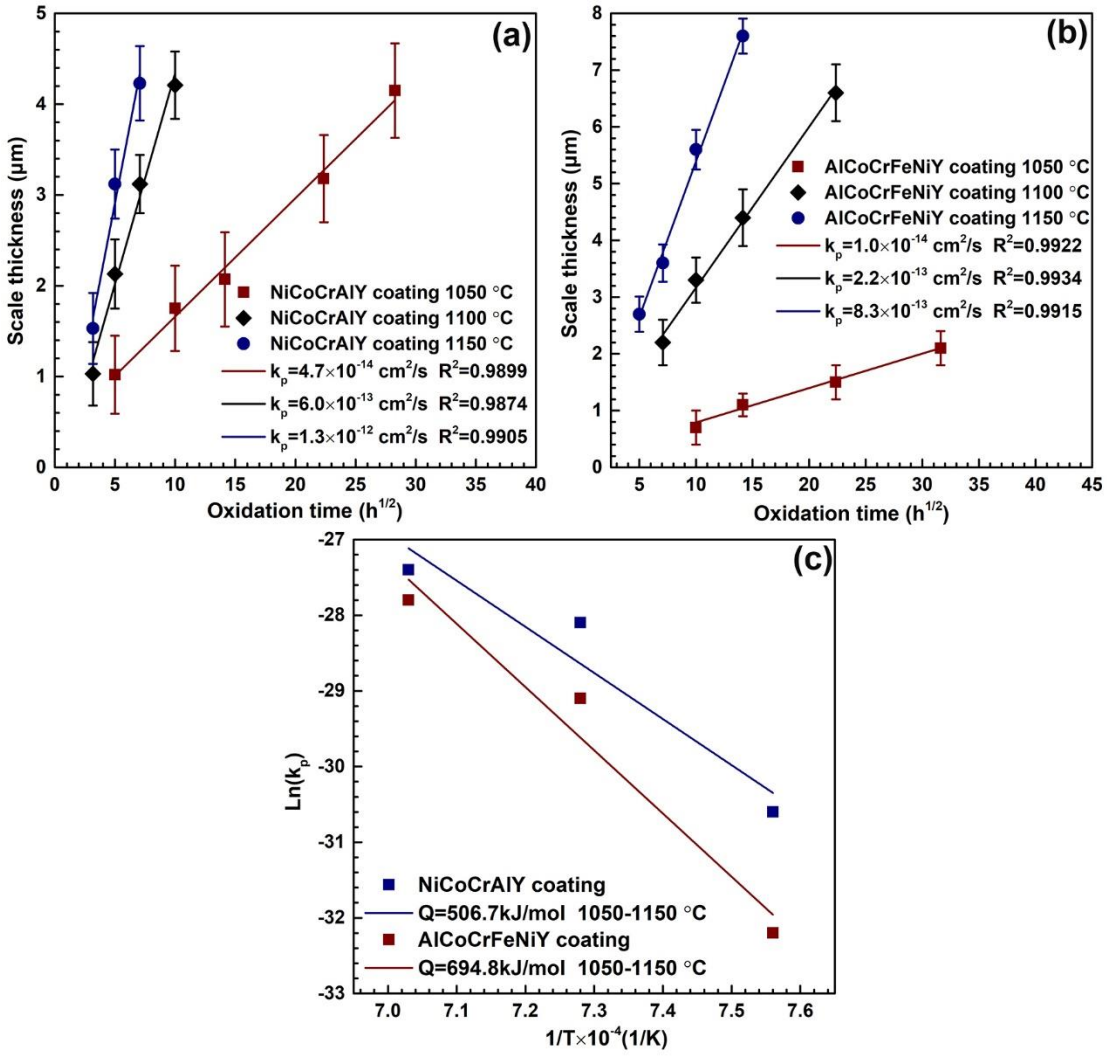

Fig. 9 Oxidation kinetics of NiCoCrAlY and AlCoCrFeNiY coatings: (a) evolution of scale thickness formed on the NiCoCrAlY coating as a function of square root of oxidation time; (b) evolution of scale thickness formed on the AlCoCrFeNiY coating as a function of square root of oxidation time; (c) activation energy for scale growth at 1050-1150 °C. (The average thickness of oxide scale is measured by ten BSE images with a magnification of 5000× and the error bar is the standard deviation. For the NiCoCrAlY coating, the measurement of scale thickness can only be performed up to a certain period of oxidation time due to the severe scale spallation afterwards.)

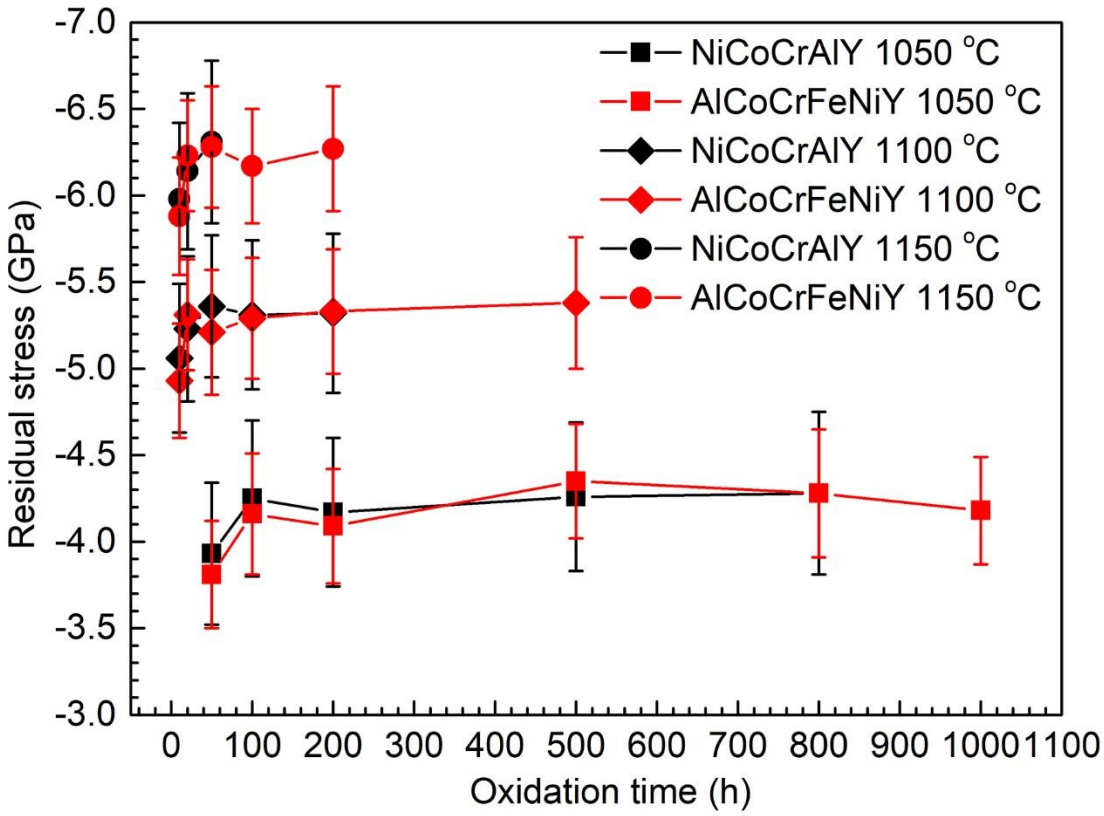

Fig. 10 Evolution of residual stress in the thermally grown alumina scales formed on the NiCoCrAlY coating and AlCoCrFeNiY coating as a function of oxidation time at 1050 °C, 1100 °C and 1150 °C. (Each solid symbol in this figure is the average value of 50 random measurements from the intact oxide scale and the error bar is the standard deviation.)

Tables

Table 1. Spray parameters for the APS process.

Spray parameters	APS
Ar flow rate (SLPM)	110
H_2 flow rate (SLPM)	17
Carrier gas flow rate (SLPM)	5
Voltage (V)	140
Current (A)	380
Gun speed (mm/s)	800
Spray distance (mm)	100

Table 2. Chemical compositions (at. %) of the γ, β and A2 phases in the AlCoCrFeNiY coating determined by STEM-EDS point analysis.

Phases	Elements (at. %)				
	Al	Co	Cr	Fe	Ni
γ	7.5±0.6	25.2±2.3	26.1±2.5	21.8±1.9	19.4±1.8
β	20.2±2.9	19.1±2.1	12.5±1.6	15.6±1.7	32.6±3.1
A2	4.1±0.4	18.9±3.1	44.3±3.3	26.1±3.2	6.6±1.1